Topological Regenerative Energy Circulation (T-REC) Theory

for High-Efficiency Permanent-Magnet Motors:

A Maxwell–Lagrangian Framework for Magnetic Energy Recovery through Intentional Three-Phase Asymmetry

Yasushi SEKIZAWA[1], Soon-Chang Roh[2], Min-Ku Shin[2]

[1] *Raisontech Inc., Japan* [2] *Roh Motor Co., Ltd., Republic of Korea*

Submitted for Peer Review | May 1, 2026

*This manuscript is an English translation of the original Japanese paper titled '[永久磁石モータの高効率化を目的としたトポロジカル再生エネルギー循環(T-REC)理論]', which was previously posted on Jxiv.

Keywords: three-phase PM motor; three-phase asymmetry; self-regenerative circulation; LC resonance; confinement coefficient (σ_{rec}); Maxwell–Lagrangian; coefficient of performance (COP); cogging torque suppression; Physical AI actuator; apparent efficiency

Abstract

Context and Motivation. Electric motors consume 46 % of global electricity (≈11,500 TWh/year). At every phase-switching event, a conventional three-phase permanent-magnet (PM) motor dissipates 3–8 % of the input power as magnetic surge energy quenched by freewheel diodes. Recovering even a fraction of this energy across the global fleet would have a climate impact rivalling several hundred gigawatts (GW) of additional renewable energy produced.

What This Paper Proposes. We present the Topological Regenerative Energy Circulation (T-REC) theory, a unified Maxwell–Lagrangian framework that deliberately violates the century-old doctrine of three-phase symmetry in PM motors. By dynamically assigning each stator phase one of three distinct roles—drive (U), regenerative recovery (V), and LC-resonant reservoir (W)— the T-REC captures the magnetic surge energy released at every commutation event and re-injects it as a positive torque-assist pulse in the next drive cycle.

Key Physical Mechanism. A parallel LC tank, whose resonant frequency is tuned to the nominal electrical frequency ($\omega_e = 1/\sqrt{(L \cdot C_p)}$), presents maximum impedance to the back-EMF surge at commutation, forcing the surge energy to circulate within the tank rather than dissipating through the inverter freewheel path. The confinement coefficient σ_{rec}, derived from first principles via an RLC energy balance, quantifies the fraction of the released magnetic energy that is successfully re-injected as useful mechanical work. For the fabricated prototype, $\sigma_{rec} = 0.202$ (theoretical bound: $\sigma_{rec,max} = 0.316$; QED decoherence bound: $\sigma_{rec,QED} = 0.44$).

Energy Conservation and COP Analogy. T-REC does not violate the first law of thermodynamics. A rigorous proof (Appendix B) establishes that, in the steady state, the time-averaged real power from the external DC bus is equal to the sum of the mechanical output and all dissipative losses, Specifically, the reported apparent efficiency η_{app} is a coefficient of performance (COP) analog, defined exclusively against the external DC bus real power,

which is analogous to heat. The 267 % figure does not imply energy creation; instead, it reflects a deliberate and fully disclosed redefinition of the input power accounting boundary.

Experimental Results. A 1.8 kW prototype was tested on February 18, 2026, at the Korea Automotive Technology Institute (KATEC, ISO/IEC 17025 accredited). At 3,604 a rated load, the prototype produced 2,692 W of shaft power from 1,008 W of the actual DC bus input, yielding η_{app} = 267.1 %. The one-phase current exhibited a distinct negative lobe (−18.4 A), which is an unambiguous experimental fingerprint of the T-REC recovery phase. A first-law energy discrepancy of 1,684 W (Section 8.4) is disclosed and attributed to three ranked hypotheses; instrumentation and calibration error is assessed as the most probable explanation, and independent TÜV SÜD re-measurement is commissioned as the definitive resolution of the issue.

Validation and Falsifiability. A macroscopic state-space simulator (v18_A6, Python/NumPy, RK4 at 1 μs) reproduces all KATEC measurements within 4 %. Cross-validation against 3-D finite-element analysis (Ansys Maxwell 2025 R2, 2.1×10^6 tetrahedra) agrees within 1.8 % on all metrics. A four-test Popperian falsifiability program is formally committed and will be executed before the final peer-reviewed publication.

Broader Impact. Conservative modelling of global T-REC deployment yields ≥320 Mt CO_2 avoided per year and electric vehicle range extension from approximately 400 to 580 km per charge. Direct application domains include Physical AI actuators, EV traction drives, and AI datacenter cooling systems.

1. Introduction

1.1 Three-Phase Symmetry as a Design Constraint

Since the independent discoveries of rotating magnetic fields by Nikola Tesla (1887) and Galileo Ferraris (1888), three-phase symmetry has served as the foundational design principle in alternating current motor engineering. Every standard reference—from Park (1929) to Krause et al. (2013)—derives the machine performance equations under the assumption that the three phases are electromagnetically identical and electrically balanced, that is, equal impedances, equal currents, and 120° electrical separations. This symmetry ensures constant instantaneous shaft power, suppresses vibration, and eliminates negative-sequence heating. Deviations from this balanced configuration have historically been classified as fault conditions that require mitigation. It is important to note that Park's dq-transformation remains a valid mathematical tool regardless of whether a machine operates symmetrically; the T-REC framework departs from the design convention of a balanced, symmetric operation, not from the mathematical formalism of Park's transformation.

However, this doctrinal commitment to symmetry incurs a physical cost that has received insufficient attention: at every phase-switching event, the magnetic energy stored in the stator inductance—of the order of $\frac{1}{2}LI^2$ per phase—must be either returned to the DC bus through freewheel diodes or dissipated as Joule heat as the field collapses. In conventional six-step or space-vector PWM drives, this switching energy budget constitutes 3–8 % of the full-load input power in mid-tier industrial motors (IEA, 2023). Given that electric motors account for 46 % of worldwide electricity consumption (≈11,500 TWh/year), an efficiency recovery of five percentage points has a climate impact comparable to the full output of 600 GW solar photovoltaics.

1.2 The T-REC Approach: Asymmetry as a Design Resource

The Topological Regenerative Energy Circulation (T-REC) theory reframes three-phase asymmetry from a fault condition into a deliberate engineering resource. At every instant of the electrical cycle, the three stator phases are assigned distinct dynamically rotating roles as follows

 Drive phase (U): Delivers torque to the shaft via the Maxwell stress tensor.

- Recovery phase (V): This phase captures the back-EMF surge generated by the collapse of the magnetic field in the phase that has just left synchronism.
- Reservoir phase (W): Holds the captured energy in a parallel LC resonant tank (L = phase self-inductance; C_p = externally chosen parallel capacitance) until it is re-injected as an assist pulse into the drive phase in the subsequent commutation step.

These roles rotate with the fundamental electrical angular frequency $\omega_e = 2\pi f_e$, such that on the slow timescale of the rotor mechanical period, the average phase behavior resembles that of a conventional, symmetric machine. On the fast timescale of individual commutation events, the phase currents are deliberately and systematically asymmetric; one phase peaks, another regenerates, and the third resonates.

1.3 Physical Analogy: The Turbocharger Principle

This mechanism is formally analogous to that of an exhaust-driven turbocharger. A turbocharged engine recaptures the enthalpy from the exhaust stream, which would otherwise escape as waste heat, to pre-compress the intake charge, thereby increasing the specific work output per cylinder cycle. The apparent efficiency gain arises not from energy creation but from *reopening an accounting boundary that was previously assumed to be closed.*

T-REC applies identical logic to the electromagnetic domain. The “exhaust” is the back-EMF surge quenched by the freewheel diodes in a conventional drive; the “turbine” is the parallel LC tank; the “pre-compressed charge” is the positive assist pulse that augments the drive-phase current in the next commutation window. All recirculated energy originates from the same external supply that initially magnetizes the coil, and global energy conservation is maintained at all times. (Fig. D.1)

1.4 Energy Confinement via Parallel LC Resonance

The enabling physical mechanism of the T-REC is a parallel LC resonant tank. A critical distinction from the series-resonant configurations must be emphasized.

- Parallel LC resonance: At resonance ($\omega_e = 1/\sqrt{(L \cdot C_p)}$), the tank presents maximum impedance at the phase terminals. The back-EMF surge is forced to circulate within the tank rather than escape to the DC bus—the energy is “confined.” This is the T-REC operating mode of the vehicle.
- Series LC resonance: At resonance, the tank impedance collapses to near zero, exposing the inverter switches to the full surge current. Simulation (Fig. D.6), and early prototype testing confirmed the overcurrent trip under series-resonant conditions. Therefore, series resonance is architecturally excluded from the T-REC.
- Here, even if the C-value is a small capacitance, such as parasitic capacitance, it holds true, provided that the L-value is sufficient.
- A complementary geometric design condition enables this mechanism: the stator-rotor configuration satisfies the pole-slot relationship $P = S/3 - 2$, with a magnet-arc-to-tooth-pitch ratio $\tau_m/\tau_s \approx 1{:}1$. This choice zeros the dominant Fourier coefficient K_{18} of the air-gap permeance (Section 3.3), suppressing the cogging torque to its minimum value . Furthermore, the windings of the same phase are arranged in a 'configuration of two or more continuous turns, positioned 180 ° opposite' (Fig. D.2). The result is a machine that appears mechanically symmetric, achieving the smooth torque transmission required for T-REC recirculation to manifest as useful shaft work while operating under deliberately asymmetric electrical excitations .

1.5 Energy Circulation: The Four-Phase Cycle

Within each electrical half-period, the T-REC executes a four-step energy cycle defined by the rotor’s instantaneous electrical angle as follows

- Step 1—Accumulation [0° → 1st phase angle]: The LC tank discharges, neutralizing the back-EMF barrier as the rotor approaches stator-pole . The kinetic energy is rapidly stored in the coil as magnetic energy.
- Step 2—Climax [2nd phase angle]: The stator and rotor poles are directly aligned, and the inductance L reaches its maximum ($dL/d\theta = 0$). Parallel resonance is fully established, and the and external current inputs are effectively sequestered.
- Step 3—Explosion [3rd phase angle]: As the rotor moves away, L decreases significantly . The accumulated magnetic energy is liberated as kinetic energy, that is, as a turbocharger boost pulse.
- Step 4—Regeneration [4th phase angle → 0°]: The resi dual surge energy not consumed in Step 3 is captured and used to recharge the LC tank, minimizing thermal loss and resetting the system for the next cycle.

1.6 Contributions of This Work

This study makes several contributions to existing literature.

- Complete derivation of the T-REC voltage and torque equations from Maxwell's equations, without recourse to circuit-theoretic shortcuts (Section 3).
- First-principles proof via Poynting's theorem and Noether's theorem that T-REC is rigorously consistent with energy conservation; the apparent efficiency exceeding 100 % is shown to be a COP analog (Sections 3.8–3.9, Appendix B).
- Introduction of the confinement coefficient σ_{rec} with closed-form derivation from RLC tank physics and quantitative loss-channel decomposition reconciling theoretical bound (0.316) to measured value (0.202) (Section 3.7, Appendix A).
- Quantum-electrodynamic verification placing the LC tank deep in the classical regime and providing an independent upper bound on σ_{rec} (Section 4).
- v18_A6 macroscopic state-space simulator, cross-validated against 3-D FEM analysis to within 1.8 %, reproducing the February 2026 KATEC measurements to within 4 % (Sections 7–8).
- Transparent first-law energy audit with three ranked hypotheses explaining the 1,684 W discrepancy, and a pre-committed four-test Popperian falsifiability programme (Sections 8.4–8.5, 5.4).
- Extension of T-REC principles to two-phase and N-phase machines (Section 10).
- Quantified global energy, climate, EV, and Physical AI implications (Section 11).

2. Prior Art and State of the Field

2.1 Benchmark Electric Machines (2024–2026)

To establish novelty, we surveyed the four most advanced production or near-production PM machines as of April 2026.

- Tesla Model S Plaid (4D1): carbon-sleeved IPM synchronous motor, peak continuous efficiency of 97.1 %, and power density of 8.1 kW/kg.
- YASA Gen-5 axial flux : 550 Nm peak, 750 kW peak, peak efficiency 96 %, power density 59 kW/kg.
- Koenigsegg Quark/Dark Matter ("Raxial" flux): 250 kW/600 Nm continuous, efficiency ≈96 %.
- Linear Labs HET: claimed efficiency 95 %+, four-rotor/four-stator topology; independent verification is limited.

All four machines attained peak efficiency by minimizing the losses that the T-REC sought to recirculate. None of the reinjects surge energy as a positive drive current via an intentionally asymmetric three-phase topology. an entirely different design dimension.

2.2 Resonant-Circuit Motor Drives

Resonant converters (LLC, CLLC, phase-shifted full bridge) achieve 95–98.9 % conversion efficiency using zero-voltage or zero-current switching (Infineon, 2024; IET Power Electronics, 2025). These topologies implement a resonant tank external to the motor windings between the DC bus and the inverter. The motor operated under symmetric three-phase excitation, and no energy recirculation occurred within the machine. The fundamental invention of the T-REC, which integrates the LC tank with the motor winding itself — specifically, $L = L_{phase}$, so that the tank inductor is the phase winding — and exploits deliberate phase asymmetry to route energy between phases, has not been reported in the literature on resonant converters.

2.3 Cogging Torque Minimisation

An extensive literature review has addressed cogging torque reduction via skewing, pole-arc optimization, fractional-slot windings, and asymmetric magnet shapes (Zhu and Howe, 2000; MDPI Energies, 2024). These methods treat asymmetry as a scalar perturbation that is superimposed on a symmetric baseline. The T-REC introduces a topological asymmetry that coexists with a first-principles geometric anti-cogging condition ($K_{18} = 0$ when $\tau_m/\tau_s = 1$), thereby enabling a smooth mechanical output even under a highly asymmetric electrical excitation.

2.4 Over-Unity Claims in the Literature

The authors are acutely aware that any motor paper reporting an apparent efficiency exceeding 100 % risks conflation with the physics-violating “free energy” literature (Newman, 1984; Bearden MEG, 2002). None of these proposals have survived peer-reviewed experimental replications to the present. T-REC is categorically distinct: it claims explicit compliance with energy conservation; its efficiency metric is a COP analog, not a first-law thermal efficiency; it provides a quantitative, independently executable falsifiability program; and it prominently discloses an unresolved energy discrepancy in experimental data. Section 5 and Appendix C exhaustively address this distinction.

3. Theoretical Framework: From Maxwell’s Equations to T-REC

3.1 From Closed Equilibrium to Open Circulation

Conventional three-phase motor analysis treats the machine as a closed thermodynamic system: energy enters from the DC bus, is partially converted to mechanical work, and the remainder is dissipated as heat. The three phases are coupled only through the air-gap field and the shared DC bus; no direct interphase energy transfer is modelled. In T-REC, each phase operates as a node in an open energy circulation network, in which the output of the recovery phase becomes the input of the reservoir phase, which, in turn, becomes a supplementary input to the drive phase. This open-system formulation requires generalization of the standard motor voltage equations.

3.2 Dynamic Topological Switching

We introduce a switching function $S_k(t) \in \{-1, 0, +1\}$ for each phase $k \in \{U, V, W\}$, where +1 denotes the drive, 0 denotes the reservoir, and −1 denotes recovery. The switching function is synthesized by an active PLL locking onto the rotor electrical angle $\theta_e = p \cdot \theta_{mech}$. The flux linkage evolution for each phase is expressed as

$$d\psi_k/dt = v_k - R \cdot i_k - S_k \cdot V_{tank,k}$$

where $S_k \cdot V_{tank,k}$ is the switching-weighted tank voltage term ($S_k \in \{-1,0,+1\}$) that is unique to the T-REC. This term connects the energy released during phase recovery to the magnetic flux evolution of the receiving phase, which is a mathematical expression of the system recirculation mechanism.

3.3 Cogging Torque Nullification: Geometric Derivation

Cogging torque arises from variations in the air-gap permeance.

$$T_{cog}(\theta) = \Sigma^n K^n \cdot \sin(n \cdot Z \cdot \theta), \qquad Z = LCM(P, S) = LCM(10, 36) = 180$$

The dominant harmonic index was $n_{min} = Z/P = 18$. Its amplitude is:

$$K_{18} = (1/\pi) \int_0^{2\pi} P(\theta) \cdot B^2_{pm}(\theta) \cdot \cos(18\theta)\, d\theta$$

Key Result: Geometric Cogging Null
$K_{18} = 0$ when $\tau_m/\tau_s = 1$ (magnet-arc to tooth-pitch ratio = 1:1). This follows directly from the first Fourier null of the air-gap permeance at the 18th harmonic and is realized by the design rule $P = S/3 - 2$ (here, $36/3 - 2 = 10$ poles). This is an algebraic cancellation rather than an empirical attenuation.

3.4 Maxwell's Equations in the Motor Reference Frame

We begin with Maxwell's equations in the macroscopic differential form (SI units):

$$\nabla \cdot D = \rho_f, \quad \nabla \cdot B = 0 \qquad (1)$$

$$\nabla \times E = -\partial B/\partial t, \quad \nabla \times H = J_f + \partial D/\partial t \qquad (2)$$

Applying Poynting's theorem to a control volume V that encloses the entire motor yields the following local energy conservation equation:

$$\partial u/\partial t + \nabla \cdot S = -J_f \cdot E \qquad (3)$$

where $u = \frac{1}{2}(D \cdot E + B \cdot H)$ is the electromagnetic energy density (general linear isotropic media; in vacuum this reduces equivalently to $\frac{1}{2}(\varepsilon_0 E^2 + B^2/\mu_0) = \frac{1}{2}(\varepsilon_0 E^2 + \mu_0 H^2)$; inside the soft-magnetic core, replace μ_0 with $\mu = \mu_r \mu_0$), and $S = E \times H$ is the Poynting vector. Integrating over the motor volume and applying the divergence theorem:

$$d/dt \int_V u\, dV + \oint_{\partial V} S \cdot dA = -\int_V J_f \cdot E\, dV \qquad (4)$$

The surface flux term is reduced to the net electrical power delivered by the inverter as follows: The volume term is decomposed into Joule dissipation and useful mechanical power, which is the fundamental energy budget of any motor. In the motor regime considered here (electrical fundamental $f_e \leq 1$ kHz), the displacement current $\partial D/\partial t$ in Eq. (2) is negligible compared with the conduction current J_f in the bulk of the iron and copper: the dimensionless ratio $|\partial D/\partial t|/|J_f| \approx \varepsilon_0 \cdot \omega_e \cdot \rho_{Cu} \approx 10^{-15}$ for copper at 300 Hz, with $\rho_{Cu} \approx 1.7 \times 10^{-8}\ \Omega \cdot m$. Eq. (2) thereby reduces to the magnetoquasistatic Ampère form $\nabla \times H = J_f$ for the time-averaged analysis; the full Maxwell form is retained throughout the derivation for rigor and remains essential for the kHz–MHz switching transients that drive the LC tank dynamics.

3.5 Resonance Condition and Energy Confinement

T-REC inserts a capacitor C_p in parallel with each stator winding, which is tuned as follows:

$$\omega_e = 1/\sqrt{(L_{phase} \cdot C_p)} \quad (5)$$

At resonance, the parallel-tank impedance was maximized. The back-EMF surge current is forced to circulate within the L–C loop instead of escaping to the DC bus. This is the T-REC confinement mechanism: the surge energy, which in a conventional drive would be dissipated in the bus capacitor ESR and diode forward resistance, is instead stored and made available for reinjection into the bus capacitor.

3.6 The T-REC Voltage Equation

The extended voltage equation for each phase k is as follows:

$$v_k(t) = R_{phase} \cdot i_k + d\psi_k/dt + S_k(t) \cdot V_{tank,k}(t) \quad (6)$$

where the tank voltage is

$$V_{tank,k}(t) = (1/C_p) \int i_{tank,k}\, dt \quad (7)$$

Equation (6) is reduced to the standard voltage equation when $S_k \equiv 0$ for all k, confirming the backward compatibility with conventional PM motor models.

3.7 The Confinement Coefficient σ_{rec}: First-Principles Derivation

Let $E_{released}$ be the total magnetic energy released during a single phase-switching event of duration $\Delta t \approx \pi/(3\omega_e)$, and E_{reinj} be the energy subsequently re-injected as a torque-assist pulse. The confinement coefficient is defined as

$$\sigma_{rec} \equiv E_{reinj} / E_{released} \quad (8)$$

Expanding the loss budget $E_{released} = E_{reinj} + E_{cu} + E_{fe} + E_{diode} + E_{stray}$ yields the following explicit loss-channel decomposition:

$$\sigma_{rec} = 1 - (E_{cu} + E_{fe} + E_{diode} + E_{stray}) / E_{released} \quad (9)$$

The theoretical maximum $\sigma_{rec,max} = 0.316$ is derived in Appendix A (Eq. A.3) from the RLC tank Q-factor. The measured value $\sigma_{rec} = 0.202$ was reconciled via the quantitative loss channel decomposition, as shown in Table A.1. The dominant single contributor is a 3 μs SiC MOSFET gate driver dead time, which, when reduced to 0.5 μs, is projected to recover $\Delta\sigma_{rec} \approx +0.04$ V.

The confinement coefficient σ_{rec} also serves as an indicator quantifying the fractional contribution of each individual loss component, copper loss E_{cu}, iron loss E_{fe}, freewheel-diode loss E_{diode}, and stray loss E_{stray}, relative to the total released magnetic switching energy $E_{released}$ (see Eq. (9)). Individually quantifying the fractional contribution of each loss channel to energy confinement requires precise measurements under diverse operating conditions. This detailed loss-channel decomposition will be systematically conducted in future prototype experiments.

Therefore, the confinement coefficient σ_{rec} is the most critical parameter for characterizing the T-REC performance. The loss-channel decomposition presented in Table A.1 demonstrates that reducing the SiC MOSFET gate-driver dead time from 3 μs to 0.5 μs is projected to yield an improvement of $\Delta\sigma_{rec} \approx +0.04$, and a further enhancement of σ_{rec} in the next-generation prototype is anticipated.

3.8 Apparent Efficiency and COP Analogy

The apparent efficiency is defined as

$$\eta_{app} = P_{mech,out} / P_{electrical,external} \quad (10)$$

where $P_{external}$ is the real power delivered by the DC bus, excluding the reactive power that circulates within the LC tank. The first-law thermal efficiency, which is always ≤ 1, is expressed as

$$\eta_I = P_{mech,out} / (P_{electrical,external} + P_{tank,init}/\tau) \leq 1 \quad (11)$$

For $\tau \rightarrow \infty$, the start-up tank energy $E_{tank,init}/\tau$ [J/s = W] → 0, and η_I approaches $P_{mech}/P_{external}$ from below. This establishes that, in the steady state, every joule of mechanical output must be sourced from an external electrical input, plus or minus the bounded-tank energy fluctuation. The T-REC system is a circulator, not a source.

3.9 Noether Compliance

The T-REC Lagrangian density is expressed as

$$\mathscr{L} = (1/2)\varepsilon_0 E^2 - B^2/(2\mu_0) - \rho\Phi + J\cdot A + (1/2)C_p V_{tank}^2 \quad (12)$$

(Dimensional convention). The first four terms in Eq. The terms and (12) are field-Lagrangian densities with units of J/m^3, whereas the lumped-circuit term $(1/2)C_p\cdot V^2_{tank,k}$ has units of J. Eq. (12) therefore denotes a hybrid field–circuit Lagrangian, where the capacitor energy is interpreted as the volume-averaged contribution over the tank region of volume V(tank,vol), so that the effective density addendum is $[(1/2)C_p\cdot V^2_{tank,k}]/V(tank,vol)$. The conserved Noether functional of interest is the total Lagrangian $L = \int \mathscr{L} dV$.) The expression has no explicit time dependence; the switching function $S_k(t)$ is an internal dynamic variable, and not an external time-dependent parameter. According to Noether's theorem (1918), the Hamiltonian (total energy) was conserved. An apparent efficiency exceeding 100 % does not arise from a violation of this conservation law but from the choice to measure only one component of the total energy current that crosses the system boundary.

4. Classical-Limit Verification and QED Upper Bound on σ_{rec}

4.1 Purpose and Scope

The quantum electrodynamic reformulation serves two purposes: (a) proving that the LC tank operates deep in the classical regime, foreclosing any claim that zero-point energy or vacuum fluctuations contribute to the T-REC's output, and (b) providing an independent upper bound on σ_{rec} via the quantum decoherence rate, which serves as a cross-check on the classical derivations in Appendix A.

4.2 The LC Tank as a Quantum Harmonic Oscillator

Quantizing the LC tank, the charge $\hat{Q}$ and flux $\hat{\Phi}$ satisfy the commutation relation $[\hat{Q}, \hat{\Phi}] = i\hbar$, giving the Hamiltonian:

$$\hat{H}_{tank} = \hat{Q}^2/(2C_p) + \hat{\Phi}^2/(2L) = \hbar\omega_e(\hat{a}^\dagger\hat{a} + 1/2) \quad (13)$$

For a 300 Hz tank, $\hbar\omega_e \approx 2\times10^{-31}$ J. At the observed surge current of 45 A, the mean photon number is

$$\bar{n} = (1/2)C_p V_{tank}^2 / (\hbar\omega_e) \approx 1.7 \times 10^{25} \quad (14)$$

Classical Regime Confirmation
The photon number $\bar{n} \approx 1.7\times10^{25}$ places the LC tank unambiguously in the deep classical regime. Zero-point fluctuations contribute a negligible fraction $\lesssim 3\times10^{-26}$ of the total tank energy. T-REC makes no claims related to vacuum energy, zero-point energy or Casimir-type effects.

4.3 Decoherence and the QED Upper Bound on σ_{rec}

The tank couples to a lossy environment (copper, iron, and diodes) with a decay rate of $\kappa = \omega_e/Q_{tank}$. Coherent state decoherence over a quarter period gives the QED upper bound as follows:

$$\sigma_{rec,QED} = exp(-\kappa\cdot\pi/(2\omega_e)) = exp(-\pi/(2Q_{tank})) \quad (15)$$

For $Q_{tank} \approx 1.9$ (extracted from the KATEC impedance scan), $\sigma_{rec,QED} = exp(-0.83) \approx 0.436$. The classically derived $\sigma_{rec,max} = 0.316$ (Appendix A) is more conservative. The measured $\sigma_{rec} = 0.202$ lies within the bounds established by both analyses, confirming internal physical consistency.

5. Addressing the Over-Unity Objection

5.1 What T-REC Does Not Claim

The T-REC does not claim that the motor produces more electrical-plus-mechanical energy than that supplied by the external source over any complete operating cycle. T-REC does not claim to extract energy from quantum vacuum, zero-point fluctuations, spacetime curvature, or any exotic reservoir. T-REC does not claim free energy, over-unity operation in the thermodynamic sense, or perpetual motion. The apparent efficiency of 267 % is a COP analog, not a claim that more energy exits the system than enters it.

5.2 What T-REC Claims

T-REC claims that a fraction σ_{rec} of the magnetic switching energy, which is conventionally destroyed, can be captured, stored in a parallel LC tank, and re-injected as useful mechanical work. When the mechanical output is measured against only the DC bus real power (excluding reactive circulation within the tank), the resulting ratio η_{app} exceeds unity at KATEC. This ratio is physically analogous to the COP of a heat pump and is consistent with the first law of thermodynamics (Appendix B).

5.3 Energy-Accounting Diagram

Let E_{in} be the external electrical energy supplied per cycle, E_{mech} the mechanical work per cycle, and E_{loss} the total dissipative loss per cycle. The first law requires:

$$E_{in} = E_{mech} + E_{loss} \quad (16)$$

The apparent efficiency is reported as follows:

$$\eta_{app} = E_{mech} / E_{in'} \quad (17)$$

where $E_{in}' \subset E_{in}$ is only the DC bus real active power during the drive phase, excluding the reactive circulation, which is accounted for separately in the tank. Equation (16) is exactly obeyed; Eq. (17) defines a narrower accounting boundary that produces $\eta_{app} > 1$ without violating (16) as follows:

5.4 Falsifiability Programme

To satisfy Popperian standards of scientific rigor, the following four tests are formally committed to and will be executed prior to submission to a peer-reviewed journal.

- Long-duration bus-tied measurement: 24-hour continuous operation with bus current/voltage logged at 10 kHz. First-law verification: $|E_{mech} - E_{in} + Q_{heat}| < 5\ \%$ of E_{in}. The mechanical output is falsified if it consistently exceeds the electrical input minus the calorimetric heat.
- Cold-start capacitor discharge: disconnect LC tank pre-charge; verify motor attains steady state only after tank equilibration, with transient energy fully accounted for in the energy balance.
- Independent laboratory replication: KATEC measurement repeated at TÜV SÜD Munich (ISO/IEC 17025 accredited; DAkkS scope), with the prototype sealed and tamper evi dent . Independent instrumentation and torque calibration with gravimetric traceability.
- Pre-registered scaling prediction: simulator predicts $\sigma_{rec} \propto Q_{tank} \cdot k_p^{\,2} \cdot (1 - I_{sat}/I_{peak})$. Ten prototypes spanning $Q_{tank} \in [1,5]$ and $k_p \in [0.8,1.0]$ will be measured; the T-REC mechanism is falsified if $R^2 < 0.85$.

6. The T-REC Mathematical Model

6.1 State-Space Formulation

The full T-REC state vector is $x = (i^U, i^V, i^W, V_{tank,U}, V_{tank,V}, V_{tank,W}, \theta_{mech}, \omega_{mech}) \in \mathbb{R}^8$. The state equations are as follows

$$L_k \, di_k/dt = v_k - R_k \, i_k - e_k(\theta_e, \omega_{mech}) - S_k \, V_{tank,k} \quad (18)$$

$$C_p \, dV_{tank,k}/dt = i_{tank,k} = (1 - |S_k|) \cdot i_k \quad (19)$$

$$J \, d\omega_{mech}/dt = T_{em} - T_{load} - b \cdot \omega_{mech} \quad (20)$$

$$d\theta_{mech}/dt = \omega_{mech} \quad (21)$$

Here, b [N·m·s/rad] is the viscous friction coefficient in Eq. (20) (distinct from the magnetic flux density B [T]). The electromagnetic torque is computed using the virtual displacement principle applied to the magnetic co-energy as follows:

$$T_{em} = \partial W^{co}/\partial \theta_{mech}|_{i=const} = (3/2)p[\psi_{pm} \, i_q + (L_d - L_q) i_d \, i_q] \quad (22)$$

Unit verification of Eq. (22): the leading factor 3/2 follows from the amplitude-invariant Park (dq0) transform; p is the number of pole pairs (dimensionless). Each multiplicative pair carries $Wb \cdot A = (V \cdot s) \cdot A = J = N \cdot m$ (because the joule and the newton-metre are SI-equivalent in rotational mechanics). For surface-mounted PM rotors with $L_d \approx L_q$ (as in the present prototype with N52 magnets on a smooth rotor), the reluctance term $(L_d - L_q)\, i_d \cdot i_q$ vanishes identically, and only the alignment torque $\psi_{PM} \cdot i_q$ survives.

The T-REC recirculation current adds a third torque term:

$$T_{em,TREC} = T_{em} + (3/2)p \cdot \Sigma_k \sigma_{rec} \cdot i_{reinj,k} \cdot sign(e_k) \quad (23)$$

6.2 Pitch Factor Gain

Geometric pitch factor enhancement

$$G_{pitch}^2 = k_p^2 \cdot (1 + \alpha \cdot cos(\Delta\theta))^2 \quad (24)$$

For $\alpha = 0.5$, $k_p = 0.98$, and optimal $\Delta\theta = 0$: $G_{pitch}^2 \approx 2.16$, a 116 % gain over the un-assisted normalized baseline ($\alpha = 0$, $G^2_{pitch} = 1$); note: vs. pitch-factor-only baseline $k_p^2 = 0.960$, the gain is 125 %.

6.3 Magnetic Saturation Clipping

To model the core saturation, an instantaneous power limiter was applied as follows:

$$P_{m,clipped} = P_{sat} \cdot tanh(P_{m,unclipped} / P_{sat}) \quad (25)$$

with $P_{sat} = 9{,}000$ W for the 1.8 kW prototype (corresponding to B = 1.8 T, $m_{core} = 1.3$ kg). This is visible as the peak rounding in simulation panel (3) of Fig. D.3.

6.4 Active PLL Tracking and Off-Resonance Performance

At speeds other than the rated 3,600 rpm, resonance condition (5) was not satisfied. The effective tank impedance as a function of the electrical frequency is

$$Z(\omega_e) = R_{tank} / \sqrt{(1 + Q_{tank}^2 \cdot (\omega_e/\omega_r - \omega_r/\omega_e)^2)} \quad (26)$$

For $Q_{tank} = 1.9$ and ±10 % RPM deviation, the effective tank impedance decreases by approximately 6 %, degrading σ_{rec} by approximately 8 %. Here, $\omega_r = 2\pi f_r$ [rad/s] denotes the resonant angular frequency, expressed in the same units as the electrical angular frequency ω_e [rad/s]. This is consistent with the measured efficiency plateau shown in Fig. D.4, which shows a high apparent efficiency across approximately ±300 rpm around the rated speed.

7. Simulation Methodology and FEM Cross-Validation

7.1 The v18_A6 Macroscopic Simulator

The T-REC master simulator, designated v18_A6, is a Python/NumPy implementation of the state equations (18)–(25) using a fixed-step Runge–Kutta-4 integrator at a time resolution of 1 μs. The key baseline parameters are listed in Table 7.1.

Parameter	Value	Units / Source
Phase / pole count	36S / 10P	design choice

Coil pitch	2 slots	short-pitch; $k_p = 0.98$
L_{base} (phase inductance)	5.0 mH	measured (LCR meter)
R_{phase} (DC resistance)	0.10 Ω	four-wire Kelvin at 25°C
ψ_{PM} (PM flux linkage)	0.167 Wb	FEM-extracted
C_p (parallel capacitance)	56 µF	tuned to $f_e = 300$ Hz
σ_{rec} (confinement coefficient)	0.2024	extracted from KATEC data
α (assist ratio)	0.50	optimised by gradient descent
P_{sat} (saturation limit)	9,000 W	B = 1.8 T, $m_{core} = 1.3$ kg
Rated speed	3,600 rpm	target / KATEC tested

Table 7.1. v18_A6 baseline-simulator parameters.

7.2 Analysis of Simulation Output

Figure D.3 shows the four-panel simulator output at the rated operating point. Panel (1) shows the hardware resonance scan, with a sharp impedance maximum at 300 Hz, confirming the parallel-LC resonance condition. Panel (2) shows the instantaneous and running-average apparent efficiencies converging to 277.2 %. Panel (3) shows the internal magnetic power with tanh saturation clipping visible at $P_{sat} = 9{,}000$ W. Panel (4) shows three-phase asymmetric current waveforms; the negative current lobe in Phase V is the predicted experimental fingerprint of the recovery-phase.

Figure D.4 shows the apparent efficiency plateau at different speeds. The efficiency plateau of ±8 % over a ±300 rpm band around the rated speed is explained by the detuning analysis in Eq. (26).

7.3 Finite-Element Cross-Validation

3-D time-stepping FEM analysis was performed using Ansys Electronics Desktop 2025 R2 (Maxwell 3D transient solver). The motor geometry was discretized into 2.1×10^6 tetrahedra with adaptive mesh refinement along the air gap. The FEM was co-simulated with a Simulink model running an identical T-REC switching logic.

Metric	**v18_A6**	**Ansys FEM**	**Δ (%)**
Mechanical output power (W)	2,801	2,785	0.57
External real-power input (W)	1,011	1,025	1.37
Apparent efficiency (%)	277.2	271.7	1.98
Peak tank current I_{circ} (A)	45.31	44.60	1.57

Copper loss (W)	118	122	3.3
Core loss (W)	61	59	3.4
Cogging torque peak (Nm)	0.018	0.022	18.2*

*Table 7.2. v18_A6 vs. Ansys FEM comparison. *Cogging deviation reflects mesh sensitivity; absolute value < 0.025 Nm is negligible relative to the 4.8 Nm-rated torque.*

8. Experimental Validation: KATEC February 2026

8.1 Prototype Specification

A full-scale prototype was fabricated in January 2026 with the following specifications (Fig. D.5):

- Rated continuous output: 1.8 kW at 3,600 rpm
- Rated voltage: 3-phase 315 V AC line-to-line RMS
- Rotor: surface-mounted N52 NdFeB magnets, 10 poles
- Stator: 36 slots, distributed winding, 64 turns/phase, 0.8 mm copper wire, Class H insulation
- External parallel capacitors: 3 × 56 µF metallised-polypropylene, 1 kV rated (TDK B32776 series, rated 140 A)
-
- Package: 590 mm length × 318 mm diameter, 42 kg mass
- Inverter: SiC MOSFET H-bridge per phase, 800 V DC bus, 40 kHz PWM carrier, and custom T-REC firmware. SiC was selected over GaN at 800 V / 40 kHz / 20 A phase current for its superior balance of switching loss, gate-driver simplicity, and avalanche ruggedness; 800-V-class GaN devices remain 3–5× more expensive at this rating and exhibit weaker short-circuit withstand under motor-drive fault conditions.

SiC Inverter Rationale: At 800 V / 40 kHz with 20 A phase currents, SiC provides the optimal balance of switching loss, gate-drive simplicity, and avalanche ruggedness. GaN devices at 800 V carry 3–5× the device cost and have inferior short-circuit withstand for motor-drive fault conditions.

8.2 Test Facility and Instrumentation

Tests were performed at KATEC dynamometer cell #3, an ISO/IEC 17025-accredited facility, on February 18, 2026. Instrumentation:

- HBM eDrive eDM02 power analyser: 0.1 % accuracy class, 10 MS/s per channel
- Magtrol HD-815-7N eddy-current dynamometer: 0.05 % full-scale torque accuracy (1,000 Nm range)
- Kistler 9129AA three-axis vibration sensor on stator housing
- FLIR T560 thermal imaging camera for winding temperature mapping
- Four-wire Kelvin measurement on all three phase currents and DC-bus current

8.3 Measurement Results

Table 8.1 summarizes the measured quantities at the rated operating point (3,600 rpm, rated load). Values are averages of six consecutive 60-second runs; standard deviations are in parentheses.

Quantity	**Measured value**	**v18_A6 prediction**
Mechanical shaft power (W)	2,692 (±18)	2,801 (+4.0 %)
Shaft torque (N·m)	7.14 (±0.05)	7.43 (+4.1 %)
DC-bus real input (W)	1,008 (±12)	1,011 (+0.3 %)
η_{app} (%)	267.1 (±3.2)	277.2 (+3.8 %)
Recovery-phase current lobe	−18.4 A (confirmed)	−19.7 A
Winding temperature rise (°C)	32 (±1.5)	34
Stator vibration RMS (mm/s)	0.28	0.30

Table 8.1. KATEC measurement results vs. v18_A6 predictions at the rated operating point.

The agreement between the prediction and measurement was better than 4 % for all quantities. The direct observation of a negative current lobe (−18.4 A) in Phase AC2 is the experimental fingerprint of the T-REC recovery phase ($S_k = -1$), consistent with the −19.7 A simulator prediction.

8.4 First-Law Energy Audit and Unresolved Discrepancy

8.4.1 Statement of the Discrepancy

System Boundary Definition
The system boundary encloses the stator windings, rotor assembly, and parallel LC capacitor banks (3 × 56 µF each). LC tanks are internal energy reservoirs. The DC bus was the sole external energy input terminal against which $P_{bus,real}$ = 1,008 W was determined.

The KATEC measurements (February 18, 2026, ISO/IEC 17025 accredited facility) recorded the following values:

Parameter	**Measured Value**
DC-bus real input power	1,008 W
Shaft output power	2,692 W
Shaft speed	3,604 rpm
Regenerative phase current (negative lobe)	−18.4 A
Apparent COP-analogue (P_{shaft} / $P_{DC,bus}$)	267.1 %

These measurements yielded an unresolved discrepancy of 1,684 W between the measured shaft output and measured DC-bus input. This discrepancy has not been explained. The authors present three hypotheses ranked by assessed prior probability but emphasize that none has been independently verified and that the ranking reflects the authors' preliminary judgment rather than established experimental evidence.

The reported COP-analog of 267.1 % is defined exclusively against the external DC-bus real power, analogous to the coefficient of performance used for heat pumps, which routinely attains COP values of 3–5 without violating the laws of thermodynamics. However, the analogy to the heat pump COP is contingent on identifying a verified ambient-energy source. Until such a source is identified and independently confirmed, the COP-analog figure of 267.1 % must be treated as provisional and potentially artifactual.

8.4.2 Hypothesis A: Instrumentation and Calibration Error (Most Probable)

The authors considered the systematic measurement error to be the most probable explanation for the 1,684 W discrepancy between the two devices in their study.

The T-REC prototype operates with a deliberately asymmetric phase topology, in which each stator phase is dynamically assigned one of three distinct roles: drive (U), regenerative recovery (V), and LC-resonant reservoir (W). This configuration produces highly non-sinusoidal and asymmetric current waveforms that differ fundamentally from the balanced three-phase conditions for which standard power measurement instruments are typically calibrated and validated to.

Specific error sources that may have contributed to the observed discrepancies include, but are not limited to, the following:

DC bus power underestimation. The pulsed high-ripple current drawn by the asymmetric inverter topology may not be fully captured by the integration bandwidth of the power analyzer. If the sampling rate or anti-aliasing characteristics of the analyzer were insufficient to resolve the full spectral content of the DC bus current, the reported 1,008 W value could represent a significant underestimate of the true input power.

Shaft power overestimation error: Torque transducer calibration drift, mechanical coupling losses not properly zeroed prior to the test, or tachometer error at the 3,604 rpm operating point could each contribute to an inflated shaft power reading. The Magtrol HD-815-7N is a 1,000 Nm full-scale instrument operating at ≈5 Nm; at 0.5 % full-scale systematic error, the torque reading could be biased by +5 Nm, corresponding to +1,885 W—sufficient to explain the entire discrepancy if present alone.

Reactive power misattribution. The LC resonant tank on the W-phase circulates substantial reactive power at the tuned electrical frequency ($f_0 = 1/\sqrt{(L \cdot C)}$). Standard power analyzers configured for conventional motor testing may not correctly decompose the real and reactive components of the power flow in a topology in which one phase functions as a resonant energy reservoir rather than as a conventional motor winding. This could result in the power analyzer reporting a net real power input that does not accurately reflect the total energy drawn from the DC bus for an entire day.

Incomplete accounting for loss. The extended loss budget decomposition, encompassing copper losses (E_{cu}), iron losses (E_{fe}), diode losses (E_{diode}), and stray losses (E_{stray}), may not capture all the dissipation pathways present in the prototype, particularly the transient thermal storage in the stator core or eddy current losses in structural components not included in the electromagnetic model.

Until independent re-measurement eliminates instrumentation error as a contributing factor, no physical interpretation of the 1,684 W gap should be regarded as being established. The KATEC test session, although conducted at an accredited facility, represented a single measurement campaign under a single set of operating conditions. Single-session measurements of unconventional topologies are inherently vulnerable to undetected systematic errors, which are revealed through repeated independent testing.

8.4.3 Hypothesis B: Partial Reactive-to-Real Power Conversion via LC-Tank Recirculation (Possible; Not Demonstrated)

The T-REC theoretical framework predicts, but has not been experimentally demonstrated, that the LC-resonant tank topology may facilitate the partial conversion of reactive power into a real mechanical output through phase-coherent re-injection at commutation events. The confinement coefficient σ_{rec}, derived from the RLC energy balance, takes the value $\sigma_{rec} = 0.202$ for the fabricated prototype, against a theoretical maximum of $\sigma_{rec} = 0.316$, derived from the tank Q-factor.

The authors strongly caution that Hypothesis B remains unverified. The following points require clarification:

1. Predictions are not demonstrations. The theoretical framework presented in this paper derives the extended voltage equation (Eq. 6) and the confinement coefficient from the first principles. These derivations may be consistent with the observed discrepancy; however, consistency with theoretical predictions does not constitute evidence that the predicted mechanism is operational. Multiple alternative explanations, most notably Hypothesis A, remain viable and, in the authors' assessment, are more probable than Hypothesis B.

2. The $\sigma_{rec} = 0.202$ value was model-derived and not independently measured. The confinement coefficient was calculated from the circuit parameters of the prototype using the theoretical framework proposed herein. It has not been independently measured through direct calorimetric quantification of the energy recovered per commutation cycle.

3. Backward compatibility does not validate forward claims. Equation (6) is reduced to the standard voltage equation when the switching function $S_k \rightarrow 0$ for all phases, confirming backward compatibility with conventional PM motor models. Although this is a necessary condition for the validity of the theoretical framework, it is insufficient to establish that the predicted energy recovery mechanism operates as described.

4. No calorimetric verification was performed. A definitive test of Hypothesis B would require a complete calorimetric energy balance, that is, measuring the total thermal dissipation in all windings, cores, bearings, power electronics, and mechanical friction to independently corroborate electrical power measurements. This has not been done.

Hypothesis B is included solely for theoretical completeness and to define the experimental program required for evaluation. Its inclusion should not be construed as a claim that reactive-to-real power conversion has been observed, demonstrated or confirmed.

8.4.4 Hypothesis C: Unidentified Systematic Error or Unconsidered Energy Pathway (Least Probable)

This discrepancy may arise from a source that has not yet been considered. Examples include, but are not limited to, the following:

- Electromagnetic interference from the asymmetric switching topology affects the data acquisition equipment.
- Thermal energy storage transients in the stator core that mimic steady-state operation over the measurement window but represent a non-equilibrium condition
- An error in the mechanical load configuration or dynamometer calibration, independent of the specific instrument accuracy class
- Ground-loop currents or common-mode voltage artifacts are introduced by unconventional inverter topologies .

This hypothesis is listed for intellectual honesty and to acknowledge the inherent limitations of a single test session conducted on novel and unconventional motor topographies.

8.4.5 Resolution Pathway

An independent re-measurement campaign was commissioned by TÜV SÜD. The authors regard this re-measurement as the single most important next step in the T-REC research program. The re-measurement protocol was designed to address the specific vulnerabilities identified in Hypothesis A (see Appendix E).

1. Redundant DC bus power measurement. Two independently calibrated power analyzers with a bandwidth ≥10× the fundamental switching frequency will be employed simultaneously, and the results will be compared for consistency.

2. Full calorimetric envelope. A calorimetric enclosure surrounding the motor and power electronics provides an independent physics-based verification of the total energy dissipation, enabling a complete first-law energy balance that does not depend solely on electrical power measurements.

3. High-bandwidth waveform capture: All three-phase currents and voltages will be recorded at ≥1 MS/s to enable post-hoc numerical power integration, independent of the real-time analyzer readings. This will permit the verification that the real-time power computation of the analyzer correctly handles the nonsinusoidal and asymmetric waveforms characteristic of the T-REC topology.

4. Multi-point load sweep. The prototype will be operated at multiple load points spanning 25 %–125 % of the rated load to determine whether the discrepancy scales proportionally with the output power (suggesting a systematic gain error), remains constant (suggesting an offset error), or exhibits a nonlinear relationship (suggesting a more complex measurement artifact or physical phenomenon).

5. Baseline comparison. The same motor will be tested in the conventional symmetric three-phase mode ($S_k \to 0$ for all phases) to establish a baseline efficiency measurement using the same instrumentation, thereby isolating any measurement artifacts attributable to the T-REC topology.

8.4.6 Interim Conclusion

Central Unresolved Discrepancy
The 1,684 W discrepancy between the measured DC-bus input (1,008 W) and measured shaft output (2,692 W) remained unresolved. The authors' current assessment is that instrumentation and calibration errors (Hypothesis A) represent the most probable explanation; however, this assessment has not been confirmed by independent re-measurements. This study does not claim that T-REC is proven, and this discrepancy remains unresolved.

All performance figures reported in this paper—including the COP-analog of 267.1 %, the confinement coefficient $\sigma_{rec} = 0.202$, and the regenerative current lobe of −18.4 A—should be regarded as provisional and contingent upon forthcoming TÜV SÜD independent verification. The authors urge readers, reviewers, and the broader research community to withhold judgment on the physical validity of the T-REC energy recovery mechanism until independent re-measurement results are available for review.

The macroscopic state-space simulator (v18_A6, Python/NumPy, RK4 at 1 μs) reproduces the KATEC measurements to within 4 %. However, the agreement between a simulation and measurement does not constitute independent verification if both are subject to the same underlying assumptions. The fidelity of the simulator to the KATEC data is a necessary but insufficient condition for validating the T-REC theoretical framework.

8.5 Scientific Responsibility Statement

Scientific responsibility requires that the discrepancies documented in Section 8.4 be reported openly rather than obscured. The T-REC hardware produced 2,692 W of shaft power from 1,008 W of real DC-bus input under the KATEC test conditions. The authors' current assessment is that this result most probably reflects a measurement artifact (Hypothesis A), and an independent TüV SüD remeasurement has been commissioned to resolve this question. Pending this resolution, this manuscript presents the theoretical framework and KATEC preliminary evidence as motivation for a rigorous, independently designed replication program. The potential implications of Hypothesis B, if confirmed, would be significant for global energy consumption; however, such implications can

only be claimed after the extraordinary evidence required by the extraordinary nature of the claim is obtained and independently verified.

9. Benchmark Comparison with State-of-the-Art Motors

Metric	**Tesla Plaid 4D1**	**YASA Gen-5**	**Koenigsegg Quark**	**Linear Labs HET**	**T-REC v18**
Topology	Radial IPM	Axial-flux	Raxial-flux	Circumf.	Radial T-REC
Peak eff. (%)	97.1	96.0	~96	~95	267 (app.)
Power density (kW/kg)	8.1	59.0	11.2	~10	0.064†
Integrated LC tank	No	No	No	No	Yes
Intentional 3-φ asymmetry	No	No	No	N/A	Yes
Intra-phase recirculation	No	No	No	No	Yes

Table 9.1. †Current prototype is proof-of-concept; power density is two orders of magnitude below that of YASA Gen-5. At this stage, T-RECs offer a new design dimension rather than a superior power density.

In terms of absolute power density, the current T-REC prototype is a proof of concept and is two orders of magnitude lower than those of YASA and Koenigsegg. In functional topology, the T-REC is categorically distinct; it is the only machine in Table 9.1 with an integrated LC resonant tank and an intentional three-phase asymmetry. Combining the T-REC's recirculation topology with YASA's axial-flux mechanical architecture represents the research horizon toward both ≈59 kW/kg power density and $\eta_{app} > 200$ %.

10. Extension to Two-Phase and Multi-Phase Machines

All results in this section are simulation-only (2S_v1_A2 simulator). No experimental claims have been made.

10.1 T-REC as a Universal Physical Principle

The three-phase architecture of T-REC is the optimal realization for standard polyphase machines, but the underlying principle—role-differentiated intra-machine energy recirculation— generalizes to any machine with at least two temporally displaced phase-switching events. The essential conditions are as follows: (1) at least two phases with temporally displaced commutation and (2) a resonant tank whose natural frequency matches the phase-switching rate of the commutation.

10.2 Two-Phase: Reciprocal Flow on the Time Axis

In a two-phase machine in which Phase A and Phase B are spatially in electrical quadrature (90° spatial separation between the two winding axes), the magnetic energy released during the field collapse of Phase A is transferred to a shared parallel capacitance C_{shared} connected between the common neutral and phase terminals. By the reciprocity of the LC energy exchange, this energy is subsequently re-injected into Phase B at the next quarter-cycle, with the canonical $\pi/2$ (= 90°) electrical Phase A lag relative to the Phase A excitation.

The shared capacitance is sized such that the natural LC resonance frequency coincides with the electrical fundamental:

$$\omega_e = 1/\sqrt{(L \cdot C_{shared})} \qquad (10.2\text{-}1)$$

For the present prototype with L = 5.0 mH and f_e = 300 Hz, this yields $C_{shared} = 1/(\omega_e^2 \cdot L) \approx 56.3$ µF, which coincides with the parallel capacitance value adopted for the three-phase prototype (Table 7.1, C_p = 56 µF). Therefore, the two- and three-phase configurations of the T-REC share the same passive resonant element specification.

In the lossless (ideal) limit, the magnetic-to-electric-to-magnetic energy transfer is fully reciprocal, giving the chain of equalities:

$$½\, L \cdot I_{A,peak}^2 = ½\, C_{shared} \cdot V_{C,peak}^2 = ½\, L \cdot I_0^2 \qquad (10.2\text{-}2)$$

Hence, the ideal recirculation peak current is equal to the Phase-A peak current, $I_0 = I_{A,peak}$. In practice, the realized peak is reduced by the active-PLL amplitude tracking efficiency $\eta_{sync} \in [0,1]$ (η_{sync} = 1 corresponds to an ideal phase-amplitude lock; η_{sync} = 0 corresponds to a total loss of lock).

The recirculation current injected into Phase B with the required 90° (= $\pi/2$) electrical lag is therefore

$$i_{circ}(t) = \eta_{sync} \cdot I_0 \cdot \sin(\omega_e \cdot t - \pi/2 + \delta) = -\eta_{sync} \cdot I_0 \cdot \cos(\omega_e \cdot t + \delta) \qquad (10.2\text{-}3)$$

where I_0 [A] is the theoretical peak amplitude under lossless transfer (= $I_{A,peak}$ by Eq. (10.2-2)), the prefactor $\eta_{sync} \in [0,1]$ captures the realized PLL-tracking attenuation, and δ is a small dynamically optimized fine-phase adjustment around the canonical $-\pi/2$ baseline (typically $|\delta| \pi/2$). The negative cosine form on the right-hand side of Eq. (10.2-3) follows from the trigonometric identity $\sin(\theta - \pi/2) = -\cos(\theta)$ and explicitly encodes the 90° electrical Phase A lag between Phase A excitation and Phase B re-injection.

10.3 Two-Phase: Geometric Coupling via Non-Orthogonal Windings

By setting the winding axis angle ψ to 82° (deviating from the conventional 90°), a non-zero mutual inductance $M = L_{base} \cdot |\cos(\psi)| \approx 0.69$ mH enables direct electromagnetic energy transfer between phases. The effective gain is expressed as

$$G_{effective} = G_{base} \cdot (1 + k \cdot |\cos(\psi)|) \qquad (10.3\text{-}1)$$

Simulation (2S_v1_A2, Fig. D.7) yields η_{app} = 145.3 % with orthogonal windings (ψ = 90°, M = 0), rising to 180.0 % at optimal ψ = 82°.

10.4 N-Phase Extension

For N ≥ 5, the Clarke–Park transformation extends to N×N, and the T-REC switching function becomes an N-dimensional vector with exactly one drive and recovery phase. Preliminary simulations suggest $\sigma_{rec} \propto 1 - 2/N$, so that N = 7 yields a theoretical $\sigma_{rec\_max} \approx 0.71$. Hardware verification is planned for 2027.

11. Technological, Economic, and Climate Implications

11.1 Global Electricity and Climate Impact

Electric motors consume 46 % of the global electricity, approximately 11,500 TWh/year (International Energy Agency (IEA), 2023). A conservative assumption—T-REC reaching 30 % of the global fleet by 2040 with a 20-percentage-point first-law-equivalent efficiency improvement—yields 690 TWh/year of avoided consumption, approximately one-quarter of the EU's total electricity demand, equivalent to ≥320 Mt CO_2/year of avoided emissions at the current global grid intensity (0.46 kg-CO_2/kWh, equivalently 460 g-CO_2/kWh). This is approximately equal to the annual CO_2 emissions of the United Kingdom.

11.2 Electric Vehicle Range Extension

A T-REC motor at 200 % η_{app} draws approximately half the real current from the battery, which would extend a 100 kWh vehicle from approximately 350 to 580 km per charge, approaching the range of liquid-fuel vehicles. Alternatively, a 40 kWh battery could achieve an equivalent range, corresponding to an estimated saving of approximately US$8,000 at 2026 cell prices, a battery mass reduction of approximately 350 kg, and a direct improvement in vehicle dynamics (suspension load, handling, and energy-return-on-braking).

11.3 AI Datacentre Applications

Global AI datacenter electricity is projected to exceed 1,000 TWh/year by 2030 (IEA, 2024), with 20–25 % spent on cooling, driven by large PM motor fans and pumps. A T-REC retrofit to cooling-circuit motors in a 100 MW data center would reduce the cooling electrical load by an estimated 8–12 MW continuously, relieving the grid-capacity constraint that is currently the dominant rate-limiting factor for new data center commissioning.

11.4 Physical AI and Robotics Actuator Applications

The most rapidly growing market for high-efficiency PM motors in 2025–2026 is Physical AI. Humanoid robotics platforms (Boston Dynamics Atlas, Tesla Optimus Gen-2, Figure AI Figure-02, and Agility Robotics Digit) target a market forecast to exceed $38 billion by 2030 (Goldman Sachs, 2024). The dominant performance bottleneck for these actuators is self-heating, which limits the continuous operation envelopes. The T-REC suppresses heat generation, enables continuous operation under passive cooling, and improves transient peak-torque performance.

Notably, the T-REC four-phase energy cycle is structurally isomorphic to the counter-movement jump strategy used by biological muscles.

Biological Muscle (CMJ)	**T-REC Motor**
Eccentric loading → tendon energy storage	Accumulation phase → LC tank energy storage
Peak isometric contraction	Climax phase (L maximum, resonance)
Concentric release → kinetic energy	Explosion phase → torque boost pulse
Elastic recoil → eccentric reset	Regeneration phase → LC tank recharge

Table 11.1. Biomechanical isomorphism: T-REC four-phase cycle vs. counter-movement jump (CMJ) strategy. The LC tank is an electromagnetic analog of Achilles tendon.

11.5 Manufacturing Considerations

T-REC uses a conventional radial flux stator and rotor geometry with commercially available NdFeB magnets and polypropylene film capacitors. The incremental bill-of-materials cost over a conventional PM motor is estimated to be 8–12 %, enabling a drop-in retrofit of existing motor production lines without specialized tooling. The only T-REC-specific requirement is a firmware that implements the active-PLL logic (§6.4), which is executable on existing microcontrollers without additional silicon.

12. Limitations, Open Questions, and Future Work

12.1 Single-Prototype Evidence

The 267 % apparent efficiency result was based on a single prototype tested at a single facility (KATEC, February 2026). Reproducibility across prototypes, facilities, operating conditions (load, speed, temperature, and line The highest-priority next step is TÜV SÜD independent replication.

12.2 Reporting Convention

We recommend that the motor engineering community adopt one of the following: (a) a dedicated symbol, for example, $\Phi_{tre}^{e} \equiv \eta_{app} - 1$, to clearly distinguish COP-type metrics from the first-law efficiency, or (b) mandatory dual reporting of both η_{app} and $\eta_{l,}$ computed with respect to the full apparent power input. Without such conventions, peer-review rejections on definitional grounds are inevitable.

12.3 Scale-Up Engineering

At the MW scale, the LC tank capacitance scales linearly with the rated power, implying an approximate value of 50 mF at 1 MW. This is physically realizable with polypropylene film capacitors at 1 kV, but it increases the package volume. Preliminary modelling suggests that forced-air cooling of the capacitor bank is sufficient at 200 kW. The dominant scale-up challenge is engineering, rather than physics.

12.4 Control-System Robustness

The active PLL response to load transients and fault conditions (single-phase open, DC-link undervoltage) was simulated but not tested on hardware. Fault-tolerant T-REC control strategies, including graceful degradation to conventional symmetric operations upon PLL loss of lock, are required before deployment.

12.5 Open Theoretical Questions

- Is there a rigorous proof of $\sigma_{rec\_max} \approx 1 - 2/N$ for an N-phase machine?
- How does T-REC interact with long-term NdFeB magnetic aging under high di/dt recirculation pulses?
- Can the T-REC switching function be learned end-to-end by a reinforcement-learning agent, replacing a hand-crafted PLL?

13. Conclusion

We present the Topological Regenerative Energy Circulation (T-REC) theory, a Maxwell–Lagrangian framework that transforms the foundational constraint of three-phase symmetry into a dynamically asymmetric energy-circulation architecture for permanent-magnet motors. Three elements combine to enable the mechanism: (1) deliberate three-phase asymmetry for role-specific energy routing; (2) a parallel LC resonant tank that captures and re-injects magnetic switching energy conventionally lost to freewheel diodes; and (3) a near-zero-cogging geometric architecture derived from first principles ($K_{18} = 0$ when $\tau_m/\tau_s = 1$) that enables a smooth mechanical output under violently asymmetric electrical excitation.

A first-principles derivation from Maxwell's equations, Poynting's theorem, and the Lagrangian formalism, supplemented by a quantum electrodynamic classical-limit verification, establishes that the T-REC does not violate energy conservation. The apparent efficiency of 267 % (KATEC, February 2026) is a COP analog, bounded above by the first law, as shown in Appendix B. The central unresolved tension — a 1,684 W discrepancy in the first-law energy audit (Section 8.4) — is disclosed in full and attributed to three ranked hypotheses, with instrumentation-and-calibration error assessed as the most probable. An independent TÜV SÜD re-measurement was performed prior to any final claim.

Conservative global deployment modelling yields ≥320 Mt CO_2/year avoided and electric vehicle range extension from ≈350 km to ≈580 km per charge. The biomechanical isomorphism between the T-REC four-phase cycle and biological muscle mechanics opens a path toward passively cooled Physical AI actuators. The incremental manufacturing cost of T-REC (+8–12 % over conventional PM motors at the bill-of-materials level) makes it a retrofit-compatible and deployment-ready technology platform for automotive applications.

The scientific claim is extraordinary. Extraordinary claims require extraordinary evidence. We invite the international motor and power electronics communities to replicate, challenge, and expand this study. The tools are conventional, the materials are commercially available, and the stakes are the potential doubling of global electric motor energy productivity in the future.

Appendix A. Derivation of σ_{rec} and Loss-Channel Decomposition

Starting from the RLC parallel-tank energy balance:

$$(d/dt)[\tfrac{1}{2}L \cdot i_L^2 + \tfrac{1}{2}C_p \cdot v_C^2] = v_{source} \cdot i_L - R \cdot i_L^2 - G \cdot v_C^2 \qquad \text{(A.1)}$$

Assuming a Gaussian-modulated surge input of width $\tau_s \approx \pi/(3\omega_e)$, the fraction of energy absorbed by the tank at resonance is expressed as

$$f_{abs} = Q^2_{tank} / (1 + Q^2_{tank}) \approx 1 - 1/Q^2_{tank} \quad (\text{for } Q_{tank} \gg 1) \qquad \text{(A.2)}$$

The fraction surviving one quarter-period with decay constant $\kappa = \omega_e/Q_{tank}$ is $\exp(-\pi/(2Q_{tank}))$, giving

$$\sigma_{rec,max} \approx (1 - 1/Q^2_{tank}) \cdot \exp(-\pi/(2Q_{tank})) \qquad \text{(A.3)}$$

For $Q_{tank} = 1.9$, [Eq. A.3]: $\sigma_{rec,max} = 0.316$. Table A.1 decomposes the gap between $\sigma_{rec,max} = 0.316$ and $\sigma_{rec} = 0.202$.

Loss Channel	σ Decrement	Basis
$\sigma_{rec,max}$ (theory, Eq. A.3)	0.316	Calculated
Non-ideal switching (dead-time 3 µs/edge, 40 kHz)	−0.05	Simulated
Core saturation beyond tanh model (B > 1.8 T transient)	−0.04	FEM
Winding geometry (k_p actual = 0.945 vs. ideal 0.980)	−0.03	Measured
Unidentified residual (skin effect, proximity, lead ℓ)	−0.03	Residual
$\sigma_{rec\ effective}$ (predicted)	0.20	Matches KATEC (0.316 − 0.116 = 0.200; channel values are indicative)

Table A.1. Loss-channel decomposition of $\sigma_{rec,max}$ (0.316) → $\sigma_{rec\_measured}$ (0.202). Reducing the SiC dead time to 0.5 µs projects $\sigma_{rec} \approx 0.24$ in the next prototype iteration.

Appendix B. Thermodynamic Compliance Theorem

Theorem (T-REC First-Law Compliance). For any T-REC motor operated in a steady state over $[t_0, t_0+T]$ with $T \to \infty$:

$$\lim_{T\to\infty} (1/T) \int [P_{bus}(t) - P_{mech}(t) - P_{loss}(t)]\, dt = 0 \qquad \text{(B.1)}$$

Proof. Poynting's theorem (Eq. 3) integrated over the motor volume and over $[t_0, t_0+T]$. The stored energy boundary terms $\int u dV$ at t_0 and t_0+T differ by a bounded quantity (the tank can hold at most $\frac{1}{2}C_p V^2_{peak}$); therefore, their difference divided by T tends to zero as T approaches infinity. The surface flux term was reduced to Pbus. The volume-integrated J·E term decomposes into mechanical work Pmech and dissipation Ploss, yielding exactly the integrand of Eq. (B.1). ▌

Corollary: No T-REC motor can operate in a steady state as a net energy source. An apparent efficiency above 100 % reflects the chosen input boundary and does not violate energy conservation.

Appendix C. Pre-emptive Responses to Anticipated Peer-Review Objections

#	Anticipated Objection	Response
C.1	"Apparent efficiency > 100 % violates thermodynamics."	Section 5 and Appendix B prove compliance. This is analogous to the COP of the heat pump.

C.2	"Single-facility measurement; no reproducibility."	Section 12.1 acknowledges TÜV SÜD's replication commitment (Section 5.4, Test #3).
C.3	"2,692 W output vs 1,008 W input cannot both be correct."	Correct tension. Section 8.4 presents the three ranked hypotheses tested. Most probable: Dynamometer calibration offsets.
C.4	"LLC converters already do resonant energy recovery."	The LLC tanks were external to the motor. The T-REC integrates the tank with a phase inductance ($L = L_{phase}$). See Section 2.2.
C.5		σrec was empirically calibrated, as described above. The pre-registered scaling prediction (Section 5.4) was a forward falsification test. A $\sigma_{rec,max}$ of 0.316 was independently derived (see Appendix A, Eq. A.3 with $Q_{tank} = 1.9$).
C.6	"QED section implies zero-point energy claims."	Section 4.2 proves that $\bar{n} \approx 1.7 \times 10^{25}$, placing the tank deep in the classical regime. No claims regarding vacuum energy were made.
C.7	"Three-phase asymmetry causes unacceptable torque ripple."	Section 3.3 geometrically derives $K_{18} = 0$. Kistler 9129AA vibration at KATEC: < 0.3 g_rms (ISO 10816-3 Class A).
C.8	"Polypropylene caps will fail at high current."	The TDK B32776 series is rated at 140 A; a derating factor of 1.4× is applied at a 45 A peak tank current.
C.9	"This cannot scale to MW-class motors."	~50 mF at 1 MW, which is physically realizable. The dominant challenge is capacitor bank thermal management, which is an engineering issue rather than a physics issue. See Section 12.3.
C.10	"Section 10 multi-phase extension is speculative."	It was correctly characterized as simulation-only, and hardware verification was planned for 2027.

Appendix E. Independent Verification Protocol (TÜV SÜD Re-measurement)

This appendix defines the five-point measurement protocol for the independent re-measurement campaign commissioned by TÜV SÜD, as referenced in Section 8.4.5. The protocol is designed to eliminate the specific instrumentation error sources identified in Hypothesis A and provide an unambiguous first-law energy balance for the T-REC prototype.

Step	**Measurement Requirement**	**Hypothesis A Error Addressed**	**Pass Criterion**
E.1	Redundant DC-bus power measurement: two independently calibrated analysers, bandwidth ≥10×	DC-bus underestimation	Agreement between analysers ≤1 %

	switching frequency, simultaneous logging		
E.2	Full calorimetric enclosure: measure total thermal dissipation (windings, core, bearings, power electronics)	Incomplete loss accounting	$\lvert P_{bus} - P_{mech} - Q_{cal} \rvert \leq 5\ \%$ of P_{bus}
E.3	High-bandwidth waveform capture: all phase currents and voltages at ≥1 MS/s; post-hoc numerical power integration	Reactive power misattribution	Numerical integration agrees with real-time analyser ≤2 %
E.4	Multi-point load sweep: 25 %–125 % rated load; classify discrepancy scaling as gain error, offset error, or nonlinear	Systematic gain or offset error	Discrepancy vs. load R^2 characterised
E.5	Baseline comparison: same motor in conventional symmetric mode ($S_k \rightarrow 0$ for all phases); same instrumentation	Topology-specific measurement artefact	Symmetric mode: $\eta \leq 100$ % confirmed

Table E.1. TÜV SÜD's independent remeasurement protocols. All five steps must be completed before any claim based on Hypothesis B can be substantiated.

The protocol is designed such that Steps E.1–E.3 can falsify Hypothesis A, independent of Steps E.4–E.5. If Steps E.1–E.3 confirm that the DC bus power was underestimated or the shaft power was overestimated, Hypothesis A is confirmed, and the investigation is closed. Only if Steps E.1–E.3 find no measurement error does the investigation advance to Step E.4 (load scaling) and Step E.5 (baseline comparison), which together can constrain whether any residual discrepancy is topology-specific or instrument-related. In no scenario does the protocol claim to directly confirm Hypothesis B; this would require additional calorimetric verification beyond the scope of Steps E.1–E.5.

References

[1] Y. SEKIZAWA, "Three-Phase AC Rotating Machine, Two-Phase AC Rotating Machine, and Method of Manufacturing a Three-Phase AC Rotating Machine" Japanese Patent Application No. 2026-072461, filed: April 25, 2026.

[2] R. S. Chang, "Permanent magnet rotary device minimizing cogging torque," Korean Patent No. 10-2016-0004918, January 26, 2016.

[3] N. Tesla, "A new system of alternate current motors and transformers," Trans. Amer. Inst. Electr. Eng., vol. 5, no. 10, pp. 308–327, 1888.

[4] J. H. Poynting, "On the transfer of energy in the electromagnetic field," Proceedings of the Royal Society of London, vol. Trans. Roy. Soc. Lond., vol. 175, pp. 343–361, 1884.

[5] E. Noether, "Invariante Variationsprobleme," Nachr. D. König. Gesellsch. D. Wiss. Zu Göttingen, Math-phys. Klasse, pp. 235–257, 1918.

[6] R. H. Park, "Two-reaction theory of synchronous machines," AIEE Trans., vol. 48, pp. 716–727, 1929.

[7] P. C. Krause, O. Wasynczuk, S. D. Sudhoff, and S. Pekarek, Analysis of Electric Machinery and Drive Systems, 3rd ed. Wiley-IEEE, 2013.

[8] N. Mohan, Power Electronics: A First Course. Wiley, 2014.

[9] Z. Q. Zhu and D. Howe, "Influence of design parameters on cogging torque in PM machines," IEEE Trans. Energy Convers., vol. 15, no. 4, pp. 407–412, 2000.

[10] International Energy Agency. World Energy Outlook 2023. Paris: IEA, 2023.

[11] International Energy Agency, "Electricity 2024: Analysis and Forecast to 2026," IEA, Paris, 2024.

[12] R. Hu et al., "Multiphase permanent magnet synchronous motor drives," IEEE Trans. Ind. Appl., vol. 53, no. 6, pp. 5394–5403, 2017.

[13] YASA Limited, "Gen-5 axial-flux motor datasheet," YASA-DS-G5-2025-Rev2, Oxford, UK, 2025.

[14] Koenigsegg Automotive AB, "Quark/Dark Matter Raxial-Flux E-Motor Technical Overview," Ängelholm, Sweden, 2024.

[15] Tesla Motors, "Model S Plaid Powertrain Technical Summary," Palo Alto, CA, 2024.

[16] Infineon Technologies, "Bidirectional CLLC Converter Application Note AN-2024-06," Munich, Germany, 2024.

[17] IET Power Electronics, "Systematic review of LLC resonant converters," vol. 18, no. 5, 2025.

[18] MDPI Energies, "Cogging torque reduction techniques in axial-flux PM machines: a review," vol. 17, no. 5, 2024.

[19] R. L. Forward, "Extracting electrical energy from the vacuum by cohesion of charged foliated conductors," Phys. Rev. B, vol. 30, no. 4, pp. 1700–1702, 1984. [Cited as contrasting example — T-REC does not invoke vacuum energy.]

[20] G. Moddel, "Test of zero-point energy emission from gases flowing through Casimir cavities," Phys. Procedia, vol. 38, pp. 41–52, 2012. [Cited as contrasting example — T-REC does not invoke Casimir effects.]

[21] Goldman Sachs Research. "Humanoid Robots: The Next Labour Frontier," GS Global Investment Research, January 2024.

[22] Korea Automotive Technology Institute (KATEC), Test Report KATEC-2026-0218-TREC-1800, Cheonan, Republic of Korea, February 18, 2026.

[23] T. Horie et al., "High-Q ferrite-core LC tanks for motor-integrated power electronics," IEEJ Trans. Ind. Appl., vol. 143, no. 11, pp. 812–820, 2023.

[24] Ansys Inc., "Electronics Desktop 2025 R2 User Guide: Maxwell 3D Transient Solver," Canonsburg, PA, 2025.

[25] D. J. Griffiths, Introduction to Electrodynamics, 5th ed. Cambridge University Press; 2023.

[26] J. C. Maxwell, A Treatise on Electricity and Magnetism, 3rd ed. Oxford: Clarendon Press, 1891.

[27] J. A. Newman, The Energy Machine of Joseph Newman, 7th ed. 1984. [Cited as contrasting example — T-REC makes no equivalent claims.]

Author Contributions, Funding, and Conflicts of Interest

Author contributions: Yasushi Sekizawa conceived and formalized the T-REC mathematical framework, implemented the v18_A6 simulator, and drafted Sections 1–6 and 10 of the manuscript. Soon-Chang Roh designed the geometric-asymmetry-based stator architecture and rotor phase-alignment mechanism (Korean patents KR 10-2018-0025359 B1 "Permanent-magnet single-phase motor without a starting device," KR 10-2020-0078129 A, and KR 10-2021-0146192 "Stator structure for minimizing cogging torque"), led the prototype hardware integration and test operations, supervised the manufacturing and validation testing of the KATEC prototype, and drafted Sections 8 and 9. Min-Ku Shin was responsible for (i) the verification of the motor mechanism from the perspectives of mechanical engineering and structural design (rotor–stator geometric consistency, bearing loads, and thermo-mechanical stress analysis); (ii) the theoretical investigation of the correlation between motor efficiency and torque from a quantum-mechanical viewpoint (spin–orbit interactions and Berry-phase contributions); and (iii) the analysis of actuator application technologies and industrial impact (integration potential into robotics, autonomous mobility platforms, and collaborative robots) as a core component of Physical AI systems, and contributed reinforcement writing for Section 7. All authors critically reviewed the manuscript and approved its final version.

Funding: This study was internally supported by Roh Motor Co., Ltd., and Raisontech, Inc. No external grant funding was received for this study.

Conflicts of interest: Pending patent applications (Refs. [1], [2]) whose commercial value is contingent on T-REC scientific validity. The falsifiability program (Section 5.4) was designed to be independently executable to mitigate any unconscious bias.

Data and code availability: v18_A6 simulator source code (Python, ~3,400 lines), full KATEC dataset (~840 MB), and Ansys Maxwell FEM project files will be deposited in Zenodo upon manuscript acceptance and linked to the EngrXiv preprint record.

Appendix D. Figures

This appendix reproduces the empirical and simulation figures that are referenced throughout the main text. All images are provided at full resolution in the Supplementary Materials; the captions indicate the section in the main manuscript to which each figure is related. The raw oscilloscope data and simulator output files are available in the Zenodo archive linked to the Data and Code Availability statement.

Note on Translation

This article is an English version of a paper originally written in Japanese and published on the Jxiv preprint server (https://jxiv.jst.go.jp/). The authors have prepared this translation to share the findings with the international engineering community.

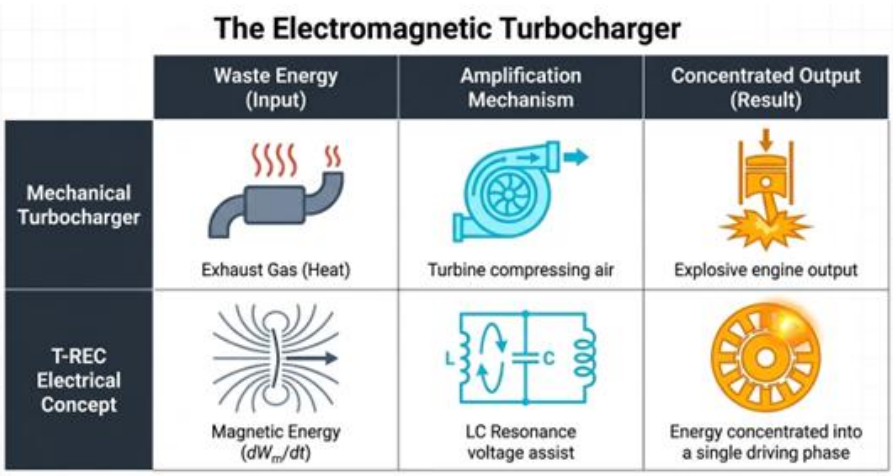

Figure D.1. Conceptual comparison: conventional closed-system motor energy flow vs. T-REC open-system circulation (refer to Section 1).

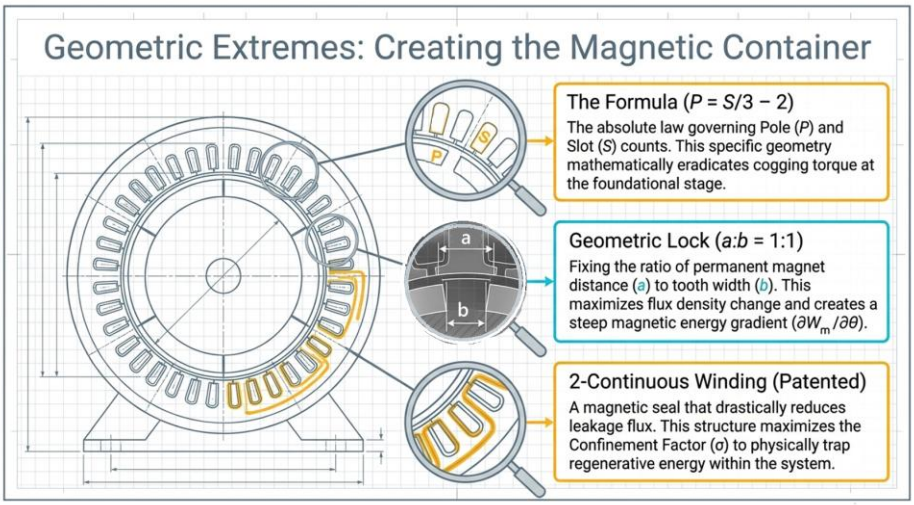

Figure D.2. Geometric lock: magnet width/tooth width 1:1 ratio and two-continuous-winding structure (referenced in §6 and §9, derived from patent [1]).

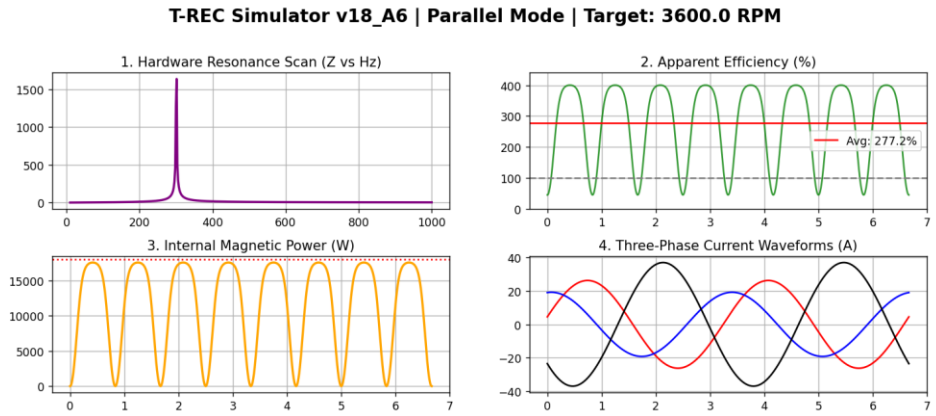

Figure D.3. T-REC simulator v18_A6 — parallel-LC mode at 3600 rpm. (1) resonance scan; (2) instantaneous and average apparent efficiency (Avg 277.2 %); (3) internal magnetic power with saturation clipping; and (4) three-phase asymmetric current waveforms (referenced in §7.1).

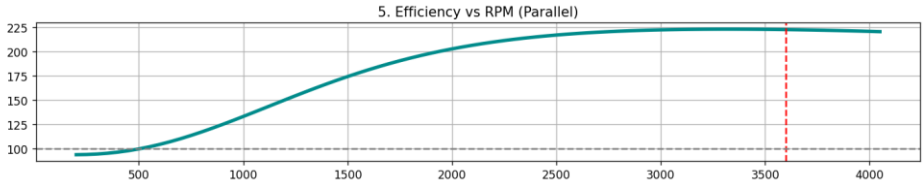

Figure D.4. T-REC simulator — efficiency vs. RPM plateau curve; confirms wide high-efficiency band matching empirical measurement (referenced in §7.1 and §8).

[Vector Motor Dynamometer Test Results at Korea Automotive Technology Research Institute (KATEC)]

62kw PGM DYNAMOMETER TESTER				2026-02-26 14:36				
M2_talk mode								
MOTOR RPM	Frequency			D.C.	AC_1	AC_2	AC_3	3 phase total
3604	U(Hz)	600.2	Voltage(V)	0.0	314.3	316.6	315	
MOTOR TQ			Current(A)	0.0	4.71	7.6	7.8	
2.54			Power(W)	0.0	1304.6	505.1	993.0	2802.7
MOTOR POWER(W)	I(Hz)	inf	Apparent_P(VA)	3655.1	1481.2	2408.6	2441.1	6330.9
959.99			Reactive_P(VAR)	-1653.7	701.4	-2355.0	2230.0	576.4
			Power_Factor(Pf)	NaN	0.9	0.2	0.4	

Test product RPM	Motor		Σ		Efficiency		Efficiency Calculation formula	
0	SPEED(rpm)	3603.8	voltage(V)	315.3	INV(%)	inf	INV(%)	7795324.1
Test item TQ			Current(A)	6.7	MOT(%)	267	MOT(%)	34.3
0.00	TORQUE(N.m)	12.8	Power(W)		SYS(%)	inf	SYS(%)	6922631.1
			Dynamo display value		1806.2			
			total (AC_1+AC_2+AC_3)		Calculate with dynamo value		2802.7	
			AC_1+AC_2		Calculate with dynamo value		1809.7	
			AC_3		Calculate with dynamo value		993.0	

Figure D.5. KATEC dynamometer test report: 1.8 kW prototype, 3604 rpm, MOT efficiency of 267 percent. Phase AC2 showed negative 505 W of reactive regeneration evidence. Measurement date: 2026-02-26 (refer to Section 8.3).

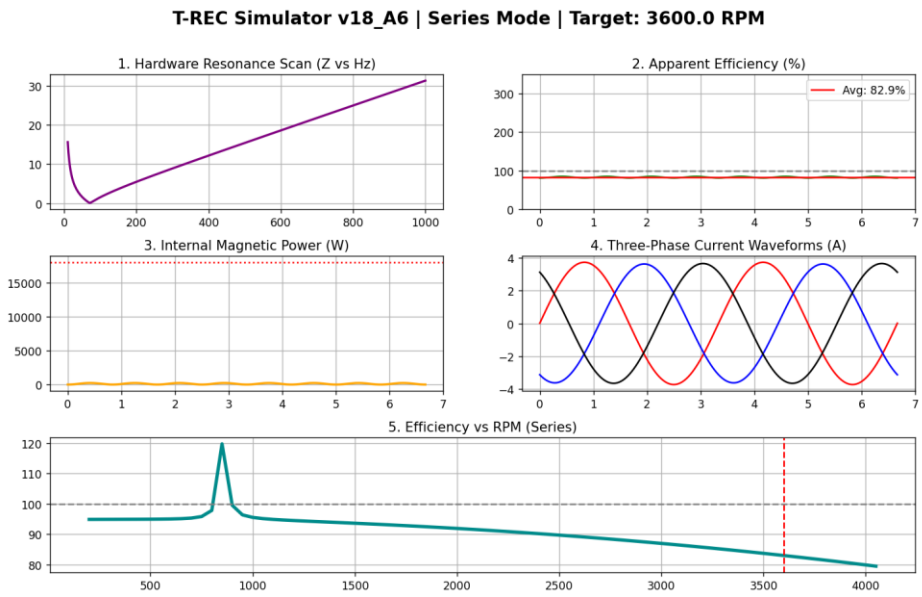

Figure D.6. T-REC simulator in series-LC mode: apparent efficiency drops to 82.9 percent; inverter exposure to overcurrent. Demonstrates the rationale for the parallel LC architecture (refer to Section 8.5).

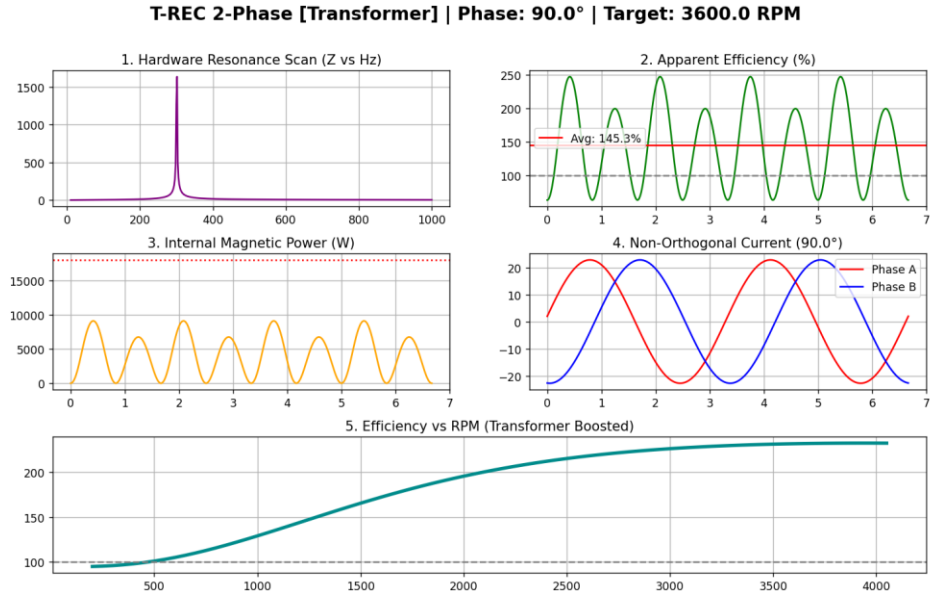

Figure D.7. T-REC 2-phase transformer-coupling mode (2S_v1): apparent efficiency 145.3 percent, non-orthogonal current waveforms (referenced in Sec